Journal of Energy Storage 71 (2023) 108151

Contents lists available at ScienceDirect

Journal of Energy Storage

journal homepage: www.elsevier.com/locate/est

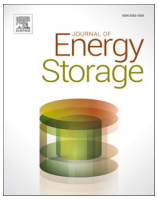

Research papers

Silicon intercalation on MXene nanosheets towards new insights into a superior electrode material for high-performance Zn-ion supercapacitor

Abdul Mateen [a,1], Zubair Ahmad [b,1], Salamat Ali [c,1], Najam Ul Hassan [d], Fahim Ahmed [d], Razan A. Alshgari [e], Mohammed Mushab [e], Sayed M. Eldin [f], Mohd Zahid Ansari [g,*], Muhammad Sufyan Javed [h,*], Kui-Qing Peng [a,*]

[a] Department of Physics and Beijing Key Laboratory of Energy Conversion and Storage Materials, Beijing Normal University, Beijing 100084, China
[b] School of Chemical Engineering, College of Engineering, Yeungnam University, Gyeongsan 38541, Republic of Korea
[c] School of Materials and Energy, Lanzhou University, Lanzhou 730000, China
[d] Department of Physics, Division of Science and Technology, University of Education, Lahore 54770, Pakistan
[e] Chemistry Department, College of Science, King Saud University, Riyadh 11451, Saudi Arabia
[f] Faculty of Engineering and Technology, Future University in Egypt, New Cairo 11835, Egypt
[g] School of Materials Science and Engineering, Yeungnam University, Gyeongsan 712749, Republic of Korea
[h] School of Physical Science and Technology, Lanzhou University, Lanzhou 730000, China

ARTICLE INFO

Keywords:
Silicon
V_2CT_x@Si nanocomposite
DFT
Zinc-ion supercapacitors

ABSTRACT

MXenes seem promising as a new two-dimensional (2D) material for energy storage and conversion applications due to their excellent conductivity, efficient accordion-like layered structure, surface chemistry, and many organized nanochannels. Nevertheless, the demonstration of MXenes' superiority is impeded by an accumulation of interlayers and the chemical sluggishness of structural components. With silicon (Si) pre intercalation techniques on V_2CT_x, MXene is able to increase its interlayer spacing and excite the outermost vanadium atoms, resulting in a frequent transfer and high storage capability of Zn-ions in supercapacitors (SCs). Motivated by the distinctive properties of Si and MXene, we have reported the V_2CT_x@Si nanocomposite electrode material for SC in this work. Si nanospheres act as spacers to intercalate into the MXene interlayers, increasing the ion transport channels while simultaneously lowering the ion transport resistance. The V_2CT_x@Si nanocomposite electrode delivers a maximum specific capacitance of 557.7 F/g at 1 A/g. The outstanding performance of the V_2CT_x@Si electrode material is demonstrated by DFT simulations, thanks to its electronic characteristics. These findings indicate that the V_2CT_x@Si possesses enhanced conductivities than the pristine MXene, which is beneficial for the rate performance of V_2CT_x@Si. The obtained E_{ads} value of the V_2CT_x@Si is −0.845 eV, higher than the pristine material (−0.652 eV), indicating energetically favorable. A zinc–ion supercapacitor (ZISC) is constructed via coupling V_2CT_x@Si as a cathode and Zn foil as an anode (denoted as V_2CT_x@Si//Zn). The V_2CT_x@Si//Zn can function at a wide potential range of 1.8 V and provide a high capacitance of 318.25 F/g at 1 A/g with a consistent cyclic life (96.4 %) up to 10,000 cycles. Furthermore, the V_2CT_x@Si//Zn possessed a maximum energy density of 143.33 Wh/kg at a power density of 900.72 W/kg, outperforming previously reported similar work.

1. Introduction

Because of the rising population and industrialization, followed by increasing pollution in the natural environment and diminishing reserves of fossil fuels, the world's climate is becoming increasingly unstable. Many studies have focused on safe, eco-friendly, simple, low-cost, and commercially feasible approaches to waste management and energy storage [1–4]. A significant emphasis is placed on the efficiency of energy storage technologies [5–7]. As a critical component of several energy storage technologies, supercapacitors (SCs) are helpful in various demanding applications that need high power for a short time or several fast charging-discharging cycles [1,8]. Significant efforts have been performed to improve the energy density of SCs without sacrificing their power density or cycling performance [9]. Excellent ion transport, good

* Corresponding authors.
E-mail addresses: zahid.smr@yu.ac.kr (M.Z. Ansari), safisabri@gmail.com (M.S. Javed), kq_peng@bnu.edu.cn (K.-Q. Peng).
[1] Equally contributed.

https://doi.org/10.1016/j.est.2023.108151
Received 7 March 2023; Received in revised form 14 May 2023; Accepted 18 June 2023
Available online 26 June 2023

electrical conductivity, and a large surface area of active materials are essential to achieve outstanding performance SCs. These advances allow for increased energy storage through the electrochemical processes at the interface of electrode-electrolyte [10]. Aqueous Zn-ion storage has received much attention as an alternative for frequent energy storage. The Zn anode's outstanding stability in aqueous electrolyte and straightforward fabrication make it an excellent choice. Developing high-performance Zn-ion supercapacitors (ZISCs) is an exciting and vital attempt [11].

Silicon has become a standard material for semiconductor-based electronic devices because of its low price, non-toxicity, tunability, and easy fabrication. Nanostructured Si is a promising material for future technological advancement. Si-based materials are important electrode materials for batteries [12] and SCs [13] fabrication. In addition, Si possesses excellent carrier mobility, which, among other benefits, expedites the accessibility of electrolytes and reduces the distances over which ions diffuse. Thus, in turn, can increase the mass transport efficiency of SCs [14–16]. Chen et al. presented a dry etched Si taper nanorod (Si-TNR) scaffold using a unique method for fabricating a new type of high energy SC electrode by integrating compactly fullerene-like carbon nanotubes, which exhibit a capacitance of 192 mF/cm^2 at 1 mV/s [17]. However, Si has low cyclic stability and oxidizes quickly in an aqueous electrolyte. Additionally, the relatively high resistance and surface reactivity of Si-based electrodes lead to low power density and poor cyclic stability [18,19]. To solve this problem, much emphasis should be paid to using different Si nanostructured materials and encapsulating Si in a matrix, particularly in two-dimensional (2D) layered materials.

MXenes are a newly discovered, fast-growing class of 2D metal carbides/nitrides [20,21]. MXene has the generic formula of $M_{n+1}X_nT_x$, where M denotes transition metal, X represents an element of carbon/nitrogen, n denotes the appropriate value (1–4), and T denotes functional groups like —F, —O, –OH. These unique materials have been fabricated when the "A" (often the 13A or 14A group element) is chemically etched out of MAX phases [22]. The exceptional surface hydrophilicity and high electrical conductivity of MXene have led to its exploration as viable electrodes [23–26]. However, the storage capacity and rate capability of SCs is negatively affected by the considerable restacking phenomena in MXene layers. It slows down the kinetics of ion transport and dramatically reduces the available sites for ion storage [27]. Several methods have been employed successfully to prevent MXene from restacking, including the fabrication of composites with other materials [28], cationic intercalation [29], and the incorporation of spacers [30]. Among these strategies, the spacer concept has garnered much interest because of its simplicity and effectiveness. In this context, polypyrrole [31], carbon nanotubes (CNTs) [32], titanium dioxide (TiO_2) [33], tin dioxide (SnO_2) [34], and graphene [25] have been used as spacers by intercalating into the MXene interlayer. This intercalation action may efficiently alleviate MXene's restacking problem, enhancing ion accessibility and electrochemical performance. While metal oxides like SnO_2 and TiO_2 may have a high resistance at the electrode-electrolyte interface, their specific capacitance is expected to be relatively low [34]. CNTs would also effectively block vertical ionic transport in MXene layers because of their tiny pores [35]. Si is predicted to hinder the reassembly of MXene by acting as spacers, enhancing the electrochemical performance. In addition, Si inclusion can enhance MXene's electrochemical activity by accelerating the surface kinetics between active sites and electrolyte ions, resulting in the enhanced performance of composite that was not possible with the pristine MXene. As a result of the vital functions that Si-based materials play and the highly abundance of these materials, high-performance SCs based on Si are still extremely desirable and need additional research and development efforts.

Motivated by the distinctive properties of Si and MXene, herein, in this study, by introducing Si nanospheres into V_2CT_x-MXene layers, V_2CT_x@Si nanocomposite was fabricated to use as a SCs electrode. Si nanospheres can act as spacers by intercalating themselves into the MXene interlayers, which enlarge the ion transport channel and lower ion transport resistance. The substantial structural stability is largely attributed to the excellent interaction of the Si nanospheres with MXene matrices. In addition, the rich surface chemistry allows Si nanospheres to be evenly distributed over MXene layers, which is helpful for preventing nanoscale Si spheres from aggregating, enhancing the charge transfer's effectiveness at the interface, and making the active material more easily accessible to the electrolyte. Benefiting from the aforementioned appealing characteristics, the sophisticated V_2CT_x@Si nanocomposite electrode with superb capacitive-like properties offers an inspirational maximum specific capacitance of 557.7 F/g at 1 A/g. The outstanding performance of the V_2CT_x@Si electrode material was demonstrated by DFT simulations thanks to its electronic characteristics. These findings demonstrate that the V_2CT_x@Si possesses enhanced conductivities than the pristine MXene, which is beneficial for the rate performance of V_2CT_x@Si. The obtained E_{ads} value of the doped material is −0.845 eV, higher than the pristine material (–0.652 eV), indicating that it is more energetically favorable. The V_2CT_x@Si electrode is the foundation for the next generation of SCs, demonstrating excellent electrochemical performance and outstanding promise for practical applications.

2. Experimental method

2.1. Synthesis of V_2CT_x-MXene

In a standard preparation method, 1 g powdered lithium fluoride (LiF) was diluted with previously prepared 9 M hydrochloric acid (30 mL). Then, 1 g of the V_2AlC-MAX phase was progressively mixed with a LiF and HCl solution. After that, the mixture was constantly agitated at 35 °C for 24 h to etch the Al layer. It was then centrifuged multiple times using ultrapure water to raise the pH of the reaction product above 6. After that, the product was sonicated for 1 h in an ice bath using an argon environment. Finally, the V_2CT_x-MXene nanosheets were extracted from the supernatant after centrifuging the mixture at 3500 rpm for 0.5 h.

2.2. Synthesis of V_2CT_x@Si nanocomposite

Typically, in the synthesis process of V_2CT_x@Si, 0.4 mmol of hexadecyl-trimethyl ammonium bromide (CTAB) was uniformly dissolved in a mixture of 40 mL deionized (DI) water and 10 mL methanol and 0.4 mL ammonium aqueous ($NH_3.H_2O$) solution (25–28 wt%). After 3 h of stirring at room temperature and adding 0.4 g of V_2CT_x-MXene, the mixture was sonicated for 5 min. Next, after the addition of 4 mmol of tetraethylorthosilicate (TEOS), the mixture was agitated for an additional 3 h. Then, placing the mixture inside an autoclave lined with Teflon and heating it at a temperature of 100 °C for 12 h, under static circumstances, the desired product of V_2CT_x@Si was achieved. To optimize the Si contents, different Si concentrations (5 %, 10 %, and 15 %) were added with V_2CT_x.

2.3. Physical characterization

Using a field emission scanning electron microscope (FESEM, HITACHI SU8220) and a transmission electron microscope (TEM, JEM-2100F, JEOL), samples were analyzed to study their morphology. To study the crystal structure of the obtained samples, X-ray diffraction (XRD) (X'Pert Pro PANalytical) with Cu Kα (with wavelength λ = 0.15406 nm) radiation was used. X-ray photoelectron spectroscopy (XPS) was used to examine the elemental composition of the prepared samples. Multimeters (DMM 7510 1/2, Keithley Instruments, USA) were used to test the electrical conductivity of samples using a four-point probe setup.

2.4. Computational details

Non spin–polarized energy calculations were performed within the framework of DFT [36] as implemented in the Vienna ab initio simulation package (VASP) [37] (version 5.4.4) with the projector augmented wave (PAW) [38]. The exchange–correlation interaction was adopted by generalized gradient approximation (GGA) with the Perdew–Burke–Ernzerhof (PBE) functional [39]. To better describe weak physical interactions, we choose a computationally cost–effective DFT–D3 method for considering van der Waals (vdW) interactions [40]. The wave function was expanded in a plane–wave basis set with periodic boundary conditions using an energy cut–off of 520 eV. The 15 Å vacuum eliminated the interlayer interactions between adjacent periodic slabs. For the numerical integration of total energy in the Brillouin zone, the Γ–centered 6 × 6 × 1 k–point mesh was used, and the geometry was supposed to converge with force lower than 0.02 eV/Å. To calculate activation barriers and find transition states, the climbing image nudged elastic band (CI–NEB) method [41] was employed as implemented in the VASP, and five images were relaxed within the NEB algorithm.

2.5. Electrochemical characterization

To conduct the electrochemical experiments, a configuration with three electrodes was used. The working electrode was composed of active material, polyvinylidene fluoride (PVDF) (which served as a binder), and conductive carbon black in the mass proportions of 80:10:10 (wt%), respectively. As a solvent to make the uniform slurry, N-Methyl-2-Pyrrolidone (NMP) was used, pasted onto 1 × 1 cm^2 piece of pre-treated carbon cloth (CC) and dried in a vacuum oven at 60 °C for 6 h. The mass accumulation of active material on the CC was approximately 1.25 mg/cm^2. The employed reference and counter electrode was Ag/AgCl and platinum wire in 1 M $ZnSO_4$ aqueous electrolyte. An electrochemical workstation (CHI 660E, China) was used for the cyclic voltammetry (CV), galvanostatic charge-discharge (GCD) and electrochemical impedance spectroscopy (EIS). All of the measurements for the CV were performed in a potential window ranging from 0.0 to 1.0 V, all of the measurements for the GCD were performed at current densities ranging from 1 to 10 A/g and EIS was measured at 0.001 to 100 kHz.

2.6. Calculations

To calculate the specific capacitance of single-electrode (C_{sp} (F/g)), the specific capacitance of ZISC (C_d (F/g)), the energy density *E* (Wh/kg), and the power density *P* (W/kg) of the ZISC are calculated according to following equations;

$$C_{sp} = \frac{I\Delta t}{m \times \Delta V} \tag{1}$$

$$C_d = \frac{I\Delta t}{M \times \Delta V} \tag{2}$$

$$E = \frac{1}{2} C_d V^2 \times \frac{1000}{3600} \tag{3}$$

$$P = \frac{E}{\Delta t} \tag{4}$$

where, I (A) is the current, Δt (s) is the discharge time, m (g) denotes the mass of the active material, M (g) shows the mass of both anode and cathode in the ZISC, and V(V) shows the potential window.

3. Results and discussion

The synthesis of V_2CT_x@Si is depicted in a simplified form, as shown in Fig. 1. First, V_2CT_x was prepared by using LiF + HCl etching to selectively exfoliate the Al layers from V_2AlC. Si nanospheres were subsequently deposited on the V_2CT_x-MXene nanosheets through TEOS hydrolysis in the presence of CTAB, yielding the V_2CT_x@Si nanocomposite. After adding Si nanospheres as spacers, the benefits of the V_2CT_x@Si nanocomposite are as follows; (i) Si nanosphere intercalate with V_2CT_x nanosheets to successfully resolve the restacking problem of V_2CT_x nanosheets, (ii) expansion of interspace can substantially boost ionic accommodation and pseudocapacitive active sites. Owing to the intercalation action, V_2CT_x@Si's electroactive sites may be easily accessible to electrolyte ions. Further, the electrical conductivity of the samples was determined, and V_2CT_x shows an electrical conductivity of 173.5 S/cm while the electrical conductivity of V_2CT_x@Si nanocomposite is increased to 310.11 S/cm. Thus, the introduction of Si into V_2CT_x enhances the electrical conductivity of the resulting sample.

The microstructure and morphology of V_2CT_x-MXene, Si nanospheres, and V_2CT_x@Si nanocomposite were investigated by using FESEM, TEM, and EDS elemental mapping. Fig. 2a depicts a FESEM image of V_2CT_x-MXene, which reveals that V_2CT_x-MXene exhibits a nanosheet-like structure with several layers restacked together. A FESEM image of Si demonstrated spherical and rod-shaped particles with a limited particle size distribution, as shown in Fig. 2c. Furthermore, the FESEM image of V_2CT_x@Si nanocomposite exhibits the nanosheets like structure with significantly increased interlayer spacing between MXene nanosheets, as illustrated in Fig. 2e. Thus, the Si nanospheres between the MXene nanosheets may drastically limit the restacking between the MXene sheets, and the electrolyte ions can

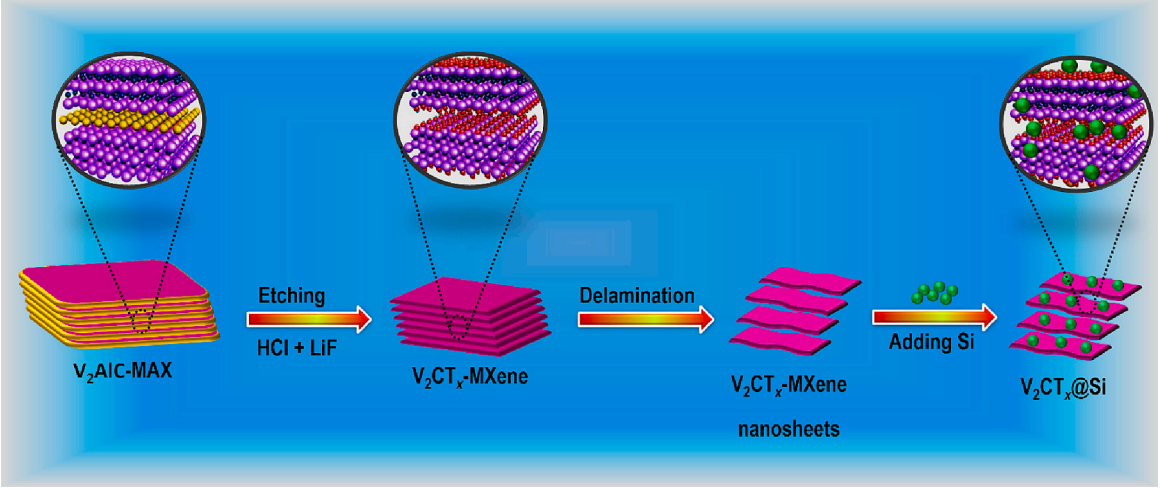

Fig. 1. Schematic depiction of synthesis of V_2CT_x@Si nanocomposite.

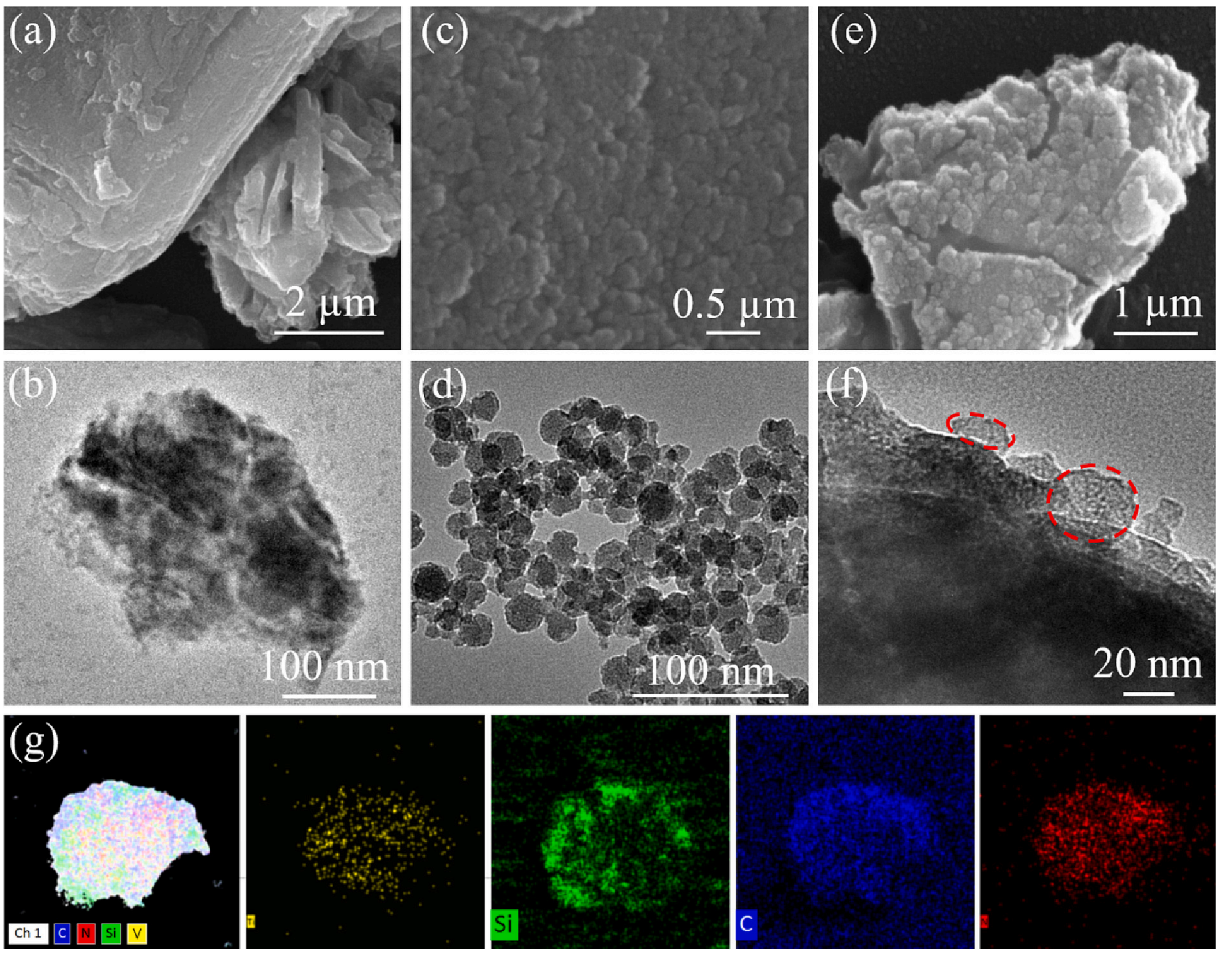

Fig. 2. FESEM images of (a) V_2CT_x-MXene; (c) Si nanospheres; (e) V_2CT_x@Si nanocomposite; TEM images of (b) V_2CT_x-MXene; (d) Si nanospheres; (f) V_2CT_x@Si nanocomposite; (g) EDS elemental mapping images of V, Si, C and N.

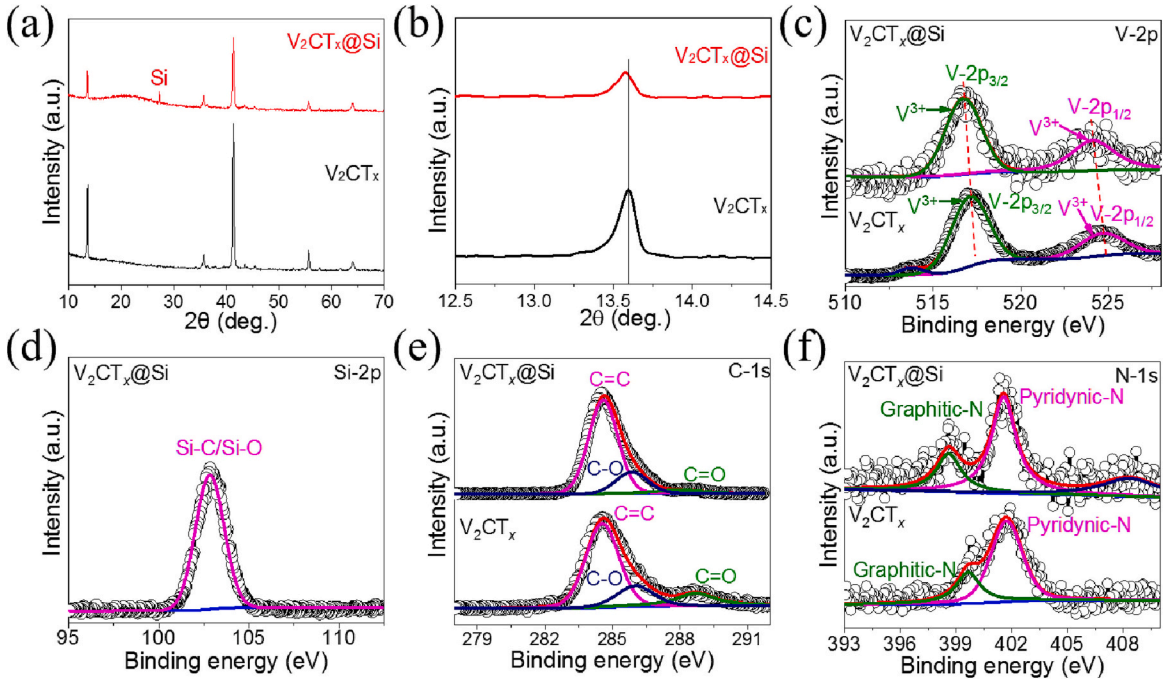

Fig. 3. (a, b) XRD patterns of V_2CT_x and V_2CT_x@Si nanocomposite; High-resolution XPS spectrum of (c) V-2p; (d) Si-2p; (e) N-1s; (f) C-1s.

readily access the electroactive regions. Hence, the V_2CT_x@Si nanocomposite demonstrates improved electrochemical performance.

Fig. 2b displays a TEM image of V_2CT_x-MXene and demonstrates the existence of translucent, thin MXene nanosheets, which eventually overlap to form a wrinkled structure. Fig. 2d demonstrates that the fabricated Si particles are spherical-shaped, with no significant size distribution. Furthermore, Fig. 2f illustrates the Si nanospheres are firmly connected to MXene nanosheets in the V_2CT_x@Si nanocomposite. It is advantageous for facilitating the interfacial charge transfer and enhancing the accessibility of electrolyte ions to the active sites. In addition, large pores are found on the surface of the V_2CT_x@Si nanocomposite, which facilitates ion transport within the nanocomposite, and thus can enhance the electrochemical performance. Additionally, the EDS elemental mapping images of V_2CT_x@Si nanocomposite are shown in Fig. 2g, which are evidence of the uniform distribution of each element. The V, Si, C, and N elemental maps confirmed the existence of V, Si, C, and N elements, indicating the V_2CT_x@Si nanocomposite was effectively formed.

The XRD patterns for V_2CT_x and V_2CT_x@Si nanocomposite are displayed in Fig. 3a, b, revealing the peaks in the V_2CT_x sample are consistent with previous reports [42,43], indicating the successful fabrication of V_2CT_x-MXene nanosheets. In the XRD patterns of V_2CT_x@Si nanocomposite, a new peak at 28.4° corresponds to (111) crystal plane of Si, suggesting the formation of V_2CT_x@Si nanocomposite. It is observed that the major peaks located at 13.6° and 41.4° of the V_2CT_x@Si nanocomposite become weaker and wider compared to pristine V_2CT_x, which may be owing to the interlayer distance modification of nanosheets generated by the Si nanospheres between the V_2CT_x-MXene nanosheets [42].

Further, XPS was used to analyze the interfacial contacts of Si with V_2CT_x in the nanocomposite material. Fig. 3c depicts the high-resolution V-2p XPS spectrum, which indicates two peaks originated from the V^{3+} signal and positioned at 517.1 eV and 524.8 eV and related to V-$2p_{3/2}$ and V-$2p_{1/2}$, respectively. However, for the V_2CT_x@Si nanocomposite sample, both peaks are shifted towards lower binding energy (the peak associated with V-$2p_{3/2}$ shifted from 517.1 eV to 516.7 and the peak related to V-$2p_{1/2}$ shifted from 524.8 eV to 524.1 eV). The relocation of peaks after the introduction of Si into V_2CT_x can be attributed to changes in the Fermi level band structure of the material [44]. Fig. 3d presents the high-resolution Si-2p XPS spectra, which reveal that the peak of the spectrum is situated at 102.4 eV. The peak was attributed to a combined contribution from Si-C and Si-O bonding and is consistent with the literature [45], suggesting the successful formation of V_2CT_x@Si nanocomposite. It is possible that the Si-O phase emerged after the sample was exposed to air, indicating Si is predominantly present as Si-O on the surface of MXene, and Si sites have a high adsorption and dissociation affinity for O_2. The majority of the adsorbed oxygen is present as amorphous SiO_2. The bonding between Si and C creates a stable hybrid framework, making it feasible to have short routes for fast ion transport and easily accessible active sites, all of which improve the pseudocapacitive performance [46]. The high-resolution C-1s XPS spectrum is illustrated in Fig. 3e. It demonstrates that the three peaks located at binding energies of 284.5, 286.1, and 288.7 eV, which ascribed to C=C, C-O, and C=O, respectively. It is possible for the covalent bonds of C-O and C-O to supply additional anchoring sites for the capturing of Si nanospheres. This would strengthen the bonding ability between Si and C, which in turn would lead to superior electrochemical performance [47]. Fig. 3f depicts the high-resolution N-1s XPS spectra for the V_2CT_x and V_2CT_x@Si nanocomposites, which exhibit two peaks. Graphite-N is associated with a binding energy of 398.6 eV, while pyridinic-N has a binding energy value of 401. 6 eV. These N-species would be responsible for serving as the primary electroactive site in the pseudocapacitance [48]. The pyridinic-N and graphitic-N play a significant part in enhancing the electrical conductivity and electrochemical activity of the V_2CT_x@Si nanocomposite.

The electrochemical performance of pristine V_2CT_x and V_2CT_x@Si nanocomposite electrodes was studied by employing a three-electrode setup within an aqueous electrolyte containing 1 M $ZnSO_4$. For the optimization of Si concentration in V_2CT_x, it is proposed to use three distinct concentrations of Si to achieve the best performance of the nanocomposite. The CV profiles of pristine V_2CT_x and all three V_2CT_x@Si nanocomposite electrodes (with 5 %, 10 %, and 15 % Si concentration) in the potential window of 0.0–1.0 V at 10 mV/s are shown in Fig. 4a. The CV profiles of pristine V_2CT_x, as well as V2CTx@Si nanocomposite with 5 % and 15 % Si concentration, is approximately rectangular shaped caused by the fast redox reactions of the cationic protons in the $ZnSO_4$ aqueous electrolyte. The CV profiles of optimized V_2CT_x@Si nanocomposite electrode (with 10 % Si concentration) outperform those of other electrodes. It indicates that, after the addition of Si nanospheres, due to the coverage of Si nanospheres on the V_2CT_x surface, a pair of redox peaks resulting from the redox reaction can be seen. The V_2CT_x@Si nanocomposite electrode shows pair of redox peaks, indicating the presence of redox reactions. Electrolyte ions intercalation and deintercalation into V_2CT_x nanosheets may be responsible for the redox peaks, as previously seen for porous Si and $Ti_3C_2T_x$ [49,50]. Further, an area under the CV profile of V_2CT_x@Si nanocomposite electrode was larger than the pristine V_2CT_x electrode. The capacitance of the V_2CT_x@Si nanocomposite electrode is significantly higher than the V_2CT_x electrode because of the excellent conductivity and interconnectivity provided by the Si nanospheres introduced between the V_2CT_x nanosheets. Comparing the pristine V_2CT_x electrode, the V_2CT_x@Si nanocomposite electrode reveals the effect of firmly and completely enclosed Si nanospheres by showing that the V_2CT_x@Si nanocomposite electrode has a much greater capacitance. Additionally, the CV profile of V_2CT_x@Si nanocomposite electrode at various scan rates (2–50 mV/s) is illustrated in Fig. 4b. Further, even at 50 mV/s, the V_2CT_x@Si nanocomposite electrode still preserved the CV profiles with a negligible shift of the cathodic and anodic peaks, which shows highly capacitive behavior with outstanding ion responsiveness and excellent rate capabilities. Furthermore, the charge storage mechanism in both pure V_2CT_x and V_2CT_x@Si nanocomposite electrodes was investigated as follows [51,52];

$$i(V) = a.v^b \tag{5}$$

$$log\ (i) = \mathrm{b}\ log\ (v) + log\ (a) \tag{6}$$

where, i represents the peak current density, v denotes the scan rate, and a and b are arbitrary constants. It is widely established that the diffusion-controlled process predominate if b = 0.5; conversely, the capacitive-controlled process predominate if b = 1.0. In accordance with the relationship between log i and log (v), the anodic and cathodic b-values for the pristine V_2CT_x electrode are 0.74 and 0.66, while the b-values for the V_2CT_x@Si nanocomposite electrode are 0.91 and 0.88, as shown in Fig. 4c. Further, Fig. 4d illustrates the capacitive and diffusion-controlled processes for pristine V_2CT_x and V_2CT_x@Si nanocomposite electrodes operating at a range of scan rates between 2 and 50 mV/s. The increasing capacitive-controlled process with increasing scan rates means that capacitance is dominated by the capacitive process, especially at high scan rates for the V_2CT_x@Si nanocomposite electrode. Additionally, Fig. 4e exhibits the V_2CT_x@Si nanocomposite electrode shows 58.3 % charge storage via diffusion-controlled process and 41.7 % via capacitive-controlled process at 10 mV/s.

Fig. 5a displays the GCD profiles of pristine V_2CT_x and V_2CT_x@Si nanocomposite electrodes at 2 A/g. The V_2CT_x@Si nanocomposite has a charge-discharge duration of 474.91 s, which is much longer than that of a pristine V_2CT_x electrode (171.55 s) at the same current density and is consistent with the CV measurements. Additionally, the GCDs of the V_2CT_x@Si nanocomposite electrode at various current densities (1–10 A/g) are illustrated in Fig. 5b. To a large degree, the GCD profiles have a symmetrical shape at each current density, which indicates excellent capacitive response and the charge–discharge process occurring at the

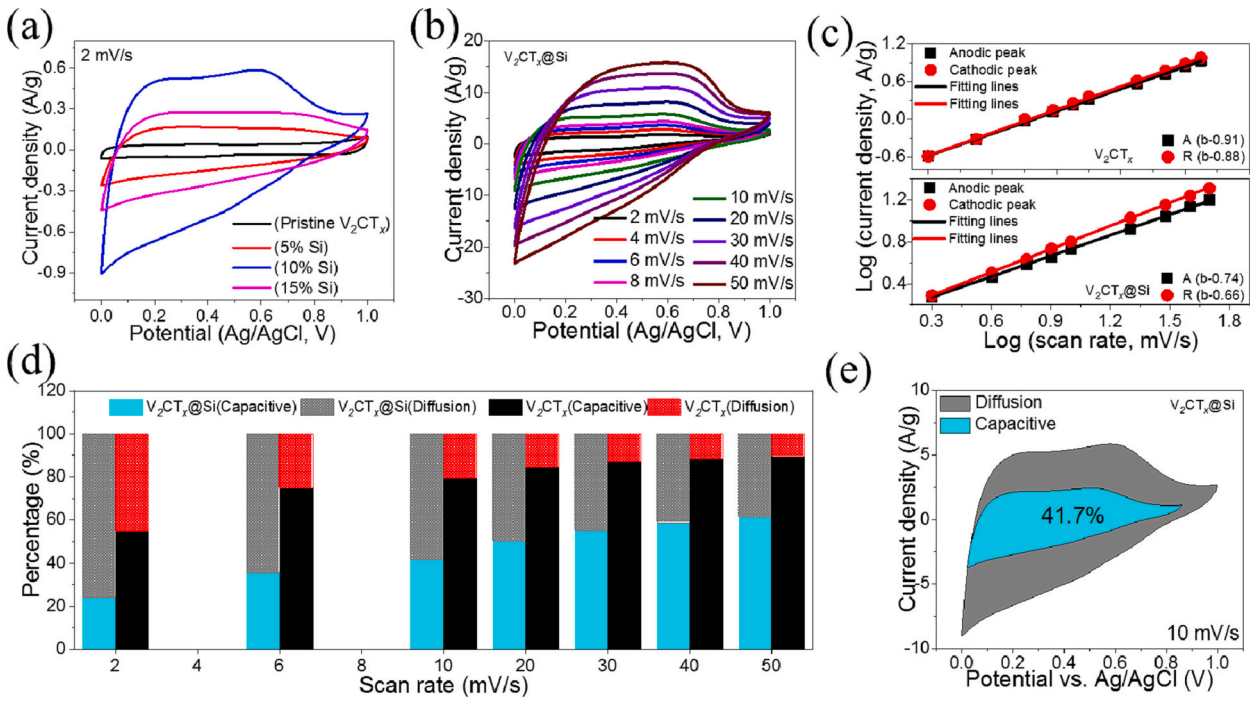

Fig. 4. (a) CVs of pristine V_2CT_x and V_2CT_x@Si nanocomposite electrodes with different concentrations of Si at 2 mV/s; (b) CVs of V_2CT_x@Si nanocomposite electrode at various scan rates; (c) *b*-value's calculations, log (*i*) versus log (*v*); (d) Contribution ratio of diffusion- and capacitive-controlled processes at a variety of scan rates; (e) Capacitive and diffusion-controlled contribution at 10 mV/s.

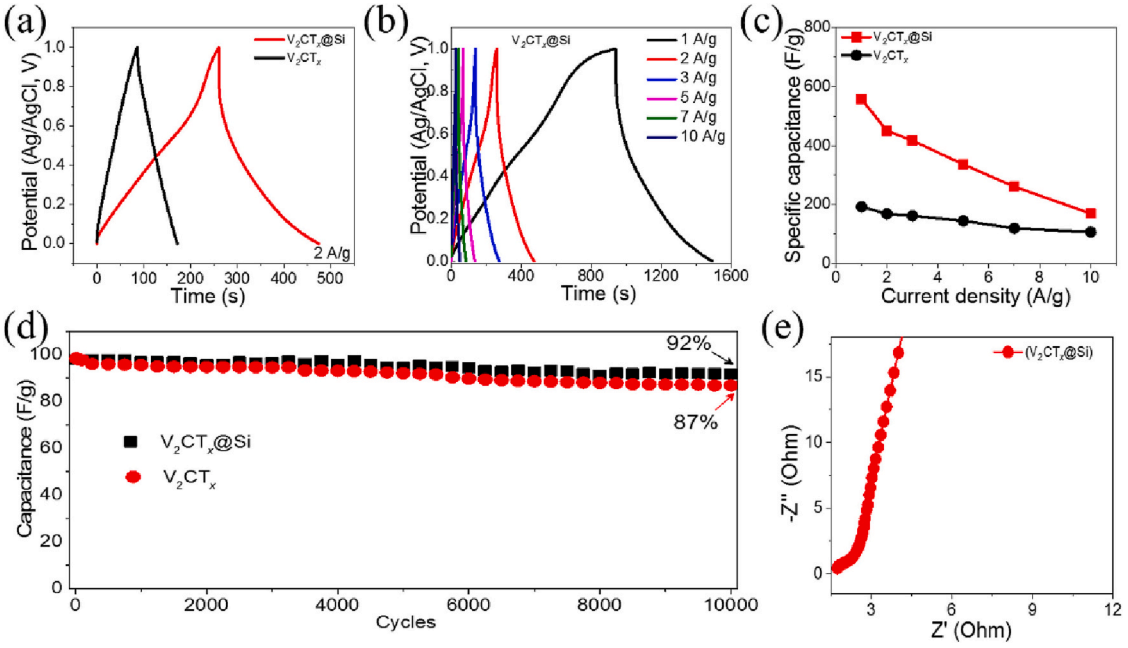

Fig. 5. (a) GCD profiles of pristine V_2CT_x and V_2CT_x@Si nanocomposite at 2 A/g; (b) GCD profiles of V_2CT_x@Si nanocomposite at various current densities; (c) Specific capacitance vs. current density; (d) Cycling stability of pristine V_2CT_x and V_2CT_x@Si nanocomposite; (e) Nyquist plot.

V_2CT_x@Si nanocomposite electrode is highly reversible. A noticeable IR drop at the start of the discharge profiles suggests the small internal resistance of V_2CT_x@Si nanocomposite electrodes [53]. The prolonged discharge time at a high value of current densities indicates exceptional charge storage properties while retaining a remarkable degree of symmetry [54]. Based on discharge time, the capacitance of the pristine V_2CT_x and V_2CT_x@Si nanocomposite electrodes was calculated. From GCDs, the capacitances of the pristine V_2CT_x and V_2CT_x@Si nanocomposite are 192 and 557.7 F/g at 1 A/g, respectively, as illustrated in Fig. 5c. Amazingly, the V_2CT_x@Si nanocomposite electrode maintains its capacitance of 169 F/g even at a high current density of 10 A/g, and is superior to that of pristine V_2CT_x (106 F/g) at the same value of current density. The higher capacitance of V_2CT_x@Si nanocomposite electrode is due to the presence of Si nanospheres between V_2CT_x nanosheets to function as spacers and inhibit the restacking of V_2CT_x nanosheets. As the cycling stability of SCs for commercial applications is

of the highest significance, extensive cycles are conducted at a high current density of 10 A/g for both V_2CT_x and V_2CT_x@Si nanocomposite electrodes. Fig. 5d shows that after 10,000 GCD cycles, the capacitance of the V_2CT_x@Si nanocomposite electrode retains ~92 % of its original value, whereas the capacitance of the V_2CT_x electrode degrades to ~87 %. This shows that the V_2CT_x@Si nanocomposite electrode maintains its exceptional energy-storage capabilities after several charge-discharge cycles. Therefore, the combination of these two materials might compensate for each other's shortcomings, thus, improving cycling stability. Furthermore, EIS experiments were carried out at open circuit potential to better understand the electrochemical performance and redox kinetics of the V_2CT_x and V_2CT_x@Si nanocomposite electrode. Fig. 5e presents a visual representation of the Nyquist plot for the V_2CT_x and V_2CT_x@Si nanocomposite electrodes. The Nyquist plot has three parts: a semicircle at high frequencies, an x-intercept, and a nearly vertical straight line at low frequencies. The x-intercept results in the equivalent series resistance (R_s), composed of the electrode's intrinsic resistance and electrolyte resistance. The semicircle's diameter represents charge transfer resistance (R_{ct}), while the slope of the vertical line represents the Warburg element and is known as electrolytic ion diffusion resistance. From the semicircle's diameter, the R_{ct} value for the V_2CT_x@Si nanocomposite electrode is 1.97 Ω. This demonstrates the remarkable electrical conductivity of the V_2CT_x@Si electrode. Thus, according to the previous investigations, the V_2CT_x@Si nanocomposite electrode displays exceptional electrochemical characteristics.

The first–principles calculations have been used to study the electronic properties of the pristine V_2CT_x, and V_2CT_x@Si to support the experimental results. Fig. 6a exhibits the optimized crystal structure of the pristine V_2CT_x, in which purple (V), brown (C), red (O), and off–white (H) atoms, respectively. The band energy and density of states (DOS) of pristine V_2CT_x are shown in Fig. 6b–c, respectively, which show metallic properties with cross states at the Fermi energy (E_F); the green dashed line shows the E_F. The band states' involvement of pristine MXene reveals that *d*–orbitals contributed for V and *p*–orbitals for C and O, where *s*–orbitals for H atoms confirm its metallic nature. The higher contribution at E_F is possessed by the V atoms, which are metals in nature, and metal atoms have higher states. Fig. S1a shows the optimized crystal structure of the pristine V_2CT_x, with Zn^{2+} insertion (silver color) in its boundary cell. Further, to observe the effects of Zn^{2+} ion on pristine material, the adsorption energy (E_{ads}), charge density difference (CDD), and diffusion energy barriers have been considered. At first, the E_{ads} of the Zn^{2+} ion have been calculated, which can reveal the energy storage capability of the material. The E_{ads} in the negative number always indicate superior thermodynamics and preferable adsorption for the substance [55]. The E_{ads} of Zn^{2+} ions are considered at the hollow site for the pristine V_2CT_x. The obtained E_{ads} value of the pristine material is −0.652 eV and the following formula has been used to calculate the E_{ads}:

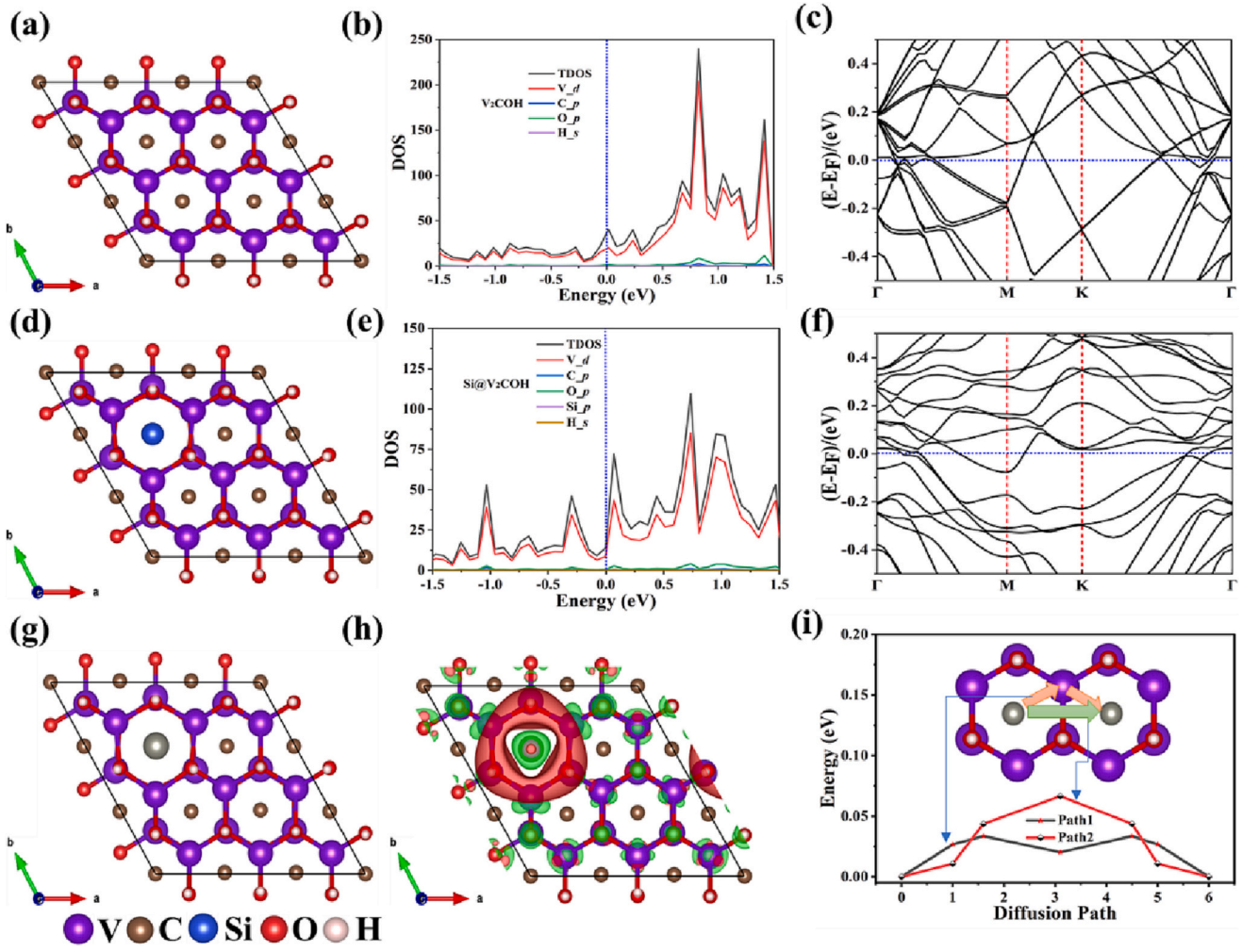

Fig. 6. (a–c) The crystal structure, band structure and DOS of pristine V_2CT_x–MXene; (d–f) The crystal structure, band structure and DOS of Si–doped V_2CT_x; (g) The crystal structure of Si–doped V_2CT_X with Zn^{2+} ion insertion; (h) CDD of Zn^{2+} ion, at the top position of V_2CT_x@Si, where red and green signify electron gain and loss, respectively; (i) The diffusion energy profiles of the Zn^{2+} ion, on V_2CT_x@Si, inset shows the paths. (For interpretation of the references to color in this figure, the reader is referred to the web version of this article.)

$$E_{ads} = E_{slab+adsorbent} - E_{slab} - E_{adsorbent} \quad (7)$$

where E_{Slab}, $E_{adsorbent}$, and $E_{Slab+adsorbent}$ are the sum of all energy produced by the optimized slab, adsorbent, and slab + adsorbent system, respectively. It is worth noting that the E_{ads} value of the system is negative, indicating that the adsorption process is energetically favorable for the material. Fig. S1b shows the CDD of Zn^{2+} ion at the hollow site of V_2CT_x along the top view, in which the red region indicates gain while green shows electron loss. The obtained result reveals that the adsorbed Zn^{2+} ion on the surface of V_2CT_x loses electrons, and V_2CT_X accepts electrons. The CDD result shows that the Zn^{2+} ion is beneficial for the V_2CT_x due to the easy sharing of charges. Fig. S1c reveals the calculated diffusion energy barriers of Zn^{2+} ions on the surface of V_2CT_x using 5 images, which have been investigated through the NEB method [41]. The diffusion paths for the mobility of Zn^{2+} ions are considered along the surface of V_2CT_x, between neighboring low–energy octahedral sites. In the initial geometry, the Zn^{2+} ion has been used in an octahedral to a neighboring octahedral position (inset of Fig. S1c) because it is energetically favorable for ions flow. The obtained energy barrier of path 1 shows a lower energy barrier (0.1 eV) than path 2 (0.2 eV). Due to path 1's low energy barrier (0.1 eV) and ease of insertion/extraction into or from the pure material, it will have favorable electrochemical characteristics.

Moreover, the Si–doping effect has also been investigated for electronic properties, E_{ads}, CDD, and diffusion energy barriers. Fig. 6d depicts the optimized crystal structure of the pristine V_2CT_x, with the Si atom shown in blue. As shown in Fig. 6e–f, the material shows dense conduction after doping the Si atom, keeping the metallic properties compared to the pristine MXene. For V_2CT_x@Si, the band structure at the Fermi level shows across band states with stronger dispersion than pristine MXene, because of the Si contribution. The DOS results also prove the same higher peaks of the doped material at E_F and justify the enhanced states due to the intercalation of Si compared to the pristine material. In V_2CT_x@Si, *d*–orbitals contributed for V, and *p*–orbitals for C, Si, and O, where s-orbitals for H atoms. It can be seen that the *d*–orbital of vanadium atoms is dominant on all other orbitals because V is a metal atom.

In conclusion, the V_2CT_x@Si shows higher electronic properties for the electrode cyclability and rate performance, and Si–doping is favorable for the electrode material. Fig. 6g shows the optimized crystal structure of V_2CT_x@Si structure with Zn^{2+} ion insertion on the top of the Si atom at the hollow site. The E_{ads} of the Zn^{+} have been calculated on V_2CT_x@Si, and it has been considered at the hollow site. The obtained E_{ads} value of the doped material is −0.845 eV, higher than the pristine material (−0.652 eV), indicating that it is more energetically favorable. Fig. 6h shows the CDD of Zn^{+} ion at the hollow site of V_2CT_x@Si along the top view, in which red and green regions indicate the gain and loss of charges. The obtained result reveals that the adsorbed Zn^{2+} ion on the surface of V_2CT_x@Si loses electrons, and V_2CT_x@Si accepts electrons. It can be seen from the charge transfer regions that the electron flow is much stronger compared to pristine materials at the surface. The CDD results show that the Si supports the easy sharing of electrons for Zn^{2+} ion, and it is more beneficial for the V_2CT_x@Si than pristine material. Further, the diffusion energy barrier of the Zn^{2+} ion on the surface of V_2CT_x@Si has been calculated. The mobility of Zn^{2+} ions has been considered following the process of pristine MXene along the surfaces. The diffusion paths are calculated using 5 images to find the energy barrier, and Fig. 6i shows the relative energy profiles of Zn^{2+} ions on the surface of V_2CT_x@Si. The inset (Fig. 6i) demonstrates the diffusion routes between neighboring low–energy octahedral sites, similar to the pristine material. The calculated results reveal that path 1 possesses a lower energy barrier of (0.035 eV) than path 2 (0.06 eV). It can be concluded that path 1 is more beneficial for the lower energy barrier compared to path 2 for pristine and V_2CT_x@Si. Compared to the energy barrier of pristine material (0.1 eV), the Si–doped material (0.035 eV) shows outstanding results with lower energy. Therefore, the Zn^{2+} ion for V_2CT_x@Si shows beneficial electrochemical properties because of its easy insertion/extraction into/from the structure.

To investigate the possible practical applications of V_2CT_x@Si nanocomposite as a cathode of full device, a ZISC (V_2CT_x@Si//Zn) was constructed using zinc-metal as anode and 1 M $ZnSO_4$ aqueous electrolyte. Fig. 7a presents a schematic depiction of the construction and operating mechanism of V_2CT_x@Si//Zn. CV measurement assessed the Zn anode and V_2CT_x@Si cathode electrochemical behaviors before ZISC assembly. A set of redox peaks can be seen for the Zn anode (Fig. 7b), which are related to stripping and depositing Zn/Zn^{2+}. A nearly rectangular-shaped CV profile of the V_2CT_x@Si cathode indicates an ideal electric double-layer capacitor response. Further, CV profiles of the V_2CT_x@Si//Zn were recorded at a constant scan rate of 10 mV/s and in various potential window ranges (Fig. 7c). According to the CV profiles recorded at various potential windows, the stable operating potential window of the V_2CT_x@Si//Zn can reach 1.8 V. The CV curve distorts when the voltage is raised above 1.8 V. Further, to extending the potential range to 2 V, the evolution of oxygen caused by electrolyte decomposition or water splitting is observable as a quick increase in current [56]. Thus, V_2CT_x@Si//Zn's potential window can be increased to 1.8 V. Further; Fig. 7d depicts the CV profiles of the V_2CT_x@Si//Zn over the potential range of 0.0–1.8 V at various scan rates ranging from 1 to 20 mV/s. All of the CV profiles continue to exhibit the presence of a visible pair of redox peaks, which is suggestive of the pseudocapacitive charge storage behavior [57]. The outstanding reversibility and stability of the V_2CT_x@Si//Zn are further evidenced by the well-preserved forms of CV profiles at high scan rates. Fig. 7e displays the GCD profiles measured over the potential range of 0.0–1.8 V and multiple current densities (1–20 A/g). Good electrochemical reversibility are shown by the almost symmetrical GCD profiles with a small voltage drop. The V_2CT_x@Si//Zn specific capacitance (C_d) can be calculated using the discharge time and total mass of active material on both anode and cathode. Fig. 7f depicts the specific capacitance as a function of current density, which reaches a maximum of 318.25, 240.94, 214.17, 172.5, 154.58, 132.22, and 122.22 F/g at 1, 2, 3, 5, 7, 10 and 20 A/g, respectively. Thus, 61.6 % of initial capacitance was retained when the current density was increased from 1 to 20 A/g, suggesting outstanding rate performance.

Further, as shown in Fig. 7g, the cycling stability of the V_2CT_x@Si//Zn was evaluated by cycling the device up to 10,000 times at a high current density of 10 A/g. Remarkably, the capacitance retention maintains at 96.4 % after 10,000 consecutive GCD cycles. These results demonstrate the exceptional cycling stability of V_2CT_x@Si//Zn.

The relevant energy and power densities were determined, and the results are shown in the Ragone plot, as shown in Fig. 8a. The V_2CT_x@Si//Zn has the maximum energy density of 143.33 Wh/kg at a power density of 900.72 W/kg and achieves 55.04 Wh/kg at 18014.4 W/kg. The high energy and power densities of V_2CT_x@Si//Zn significantly outperform those of recently reported SCs and ZISCs, in particular BCN//Zn (119.7 Wh/kg at 890 W/kg) [58], MXene/rGO//Zn (34.9 Wh/kg at 279.9 W/kg) [59], N-$Ti_2C_3T_x$-MXene//Zn (16.7 Wh/kg at 6004.8 W/kg) [60], rGO-POM//MXene-HSC (25.46 Wh/kg and 2800 W/kg) [61], and V_2CT_x/NiV-LDH//AC [62] and also listed in the Ragone plot. Based on the above-described analysis and characterization, we provide a plausible charge storage mechanism for the V_2CT_x@Si in $ZnSO_4$, as shown in Fig. 8b. The V_2CT_x@Si nanocomposite may be used for its high pseudocapacitive charge storage due to its vast effective surface area and surface redox reactions. According to DFT calculations and the charge storage mechanism, the outstanding performance of the V_2CT_x@Si electrode can be attributed to: (i) Si nanospheres' redox pseudocapacitance charge storage served as a high energy source, while the V_2CT_x nanosheet-like structure offered electrochemical double layer type charge storage with improved power density and cycle life. (ii) In the V_2CT_x@Si electrode, the intercalation of Si into 2D-V_2CT_x nanosheets gives synergistic benefits of nanostructure and increases the surface area, resolves the restacking issue of pristine V_2CT_x and both of

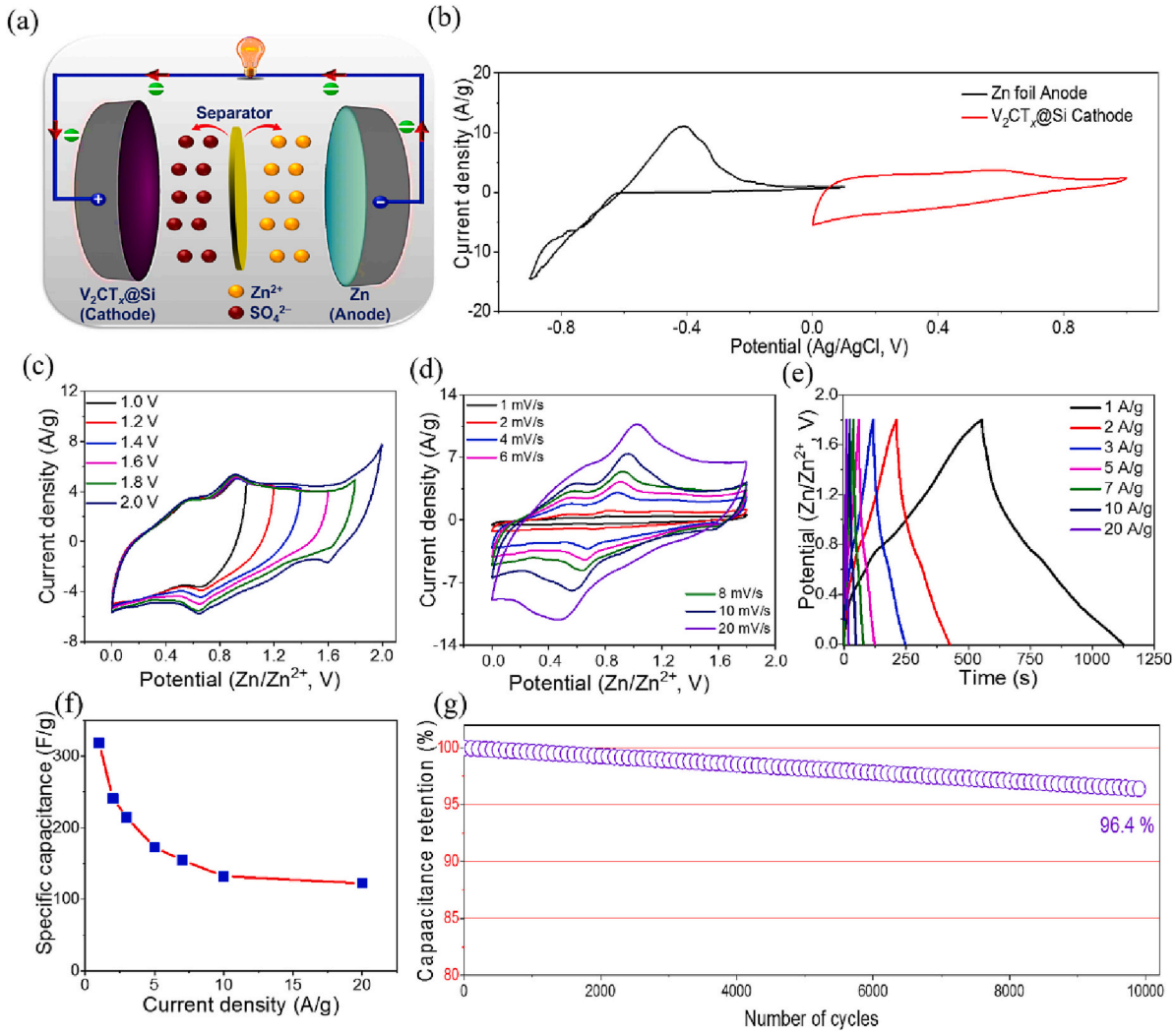

Fig. 7. Electrochemical characterization of V_2CT_x@Si//Zn device in $ZnSO_4$ electrolyte: (a) Schematic diagram of working functionality; (b) CV profiles of an anode (Zn foil) and cathode (V_2CT_x@Si); (c) CV profiles of V_2CT_x@Si//Zn device at various potential windows; (d) CV profiles at various scan rates; (e) GCD profiles at various current densities; (f) Specific capacitance as a function of current density; (g) Cycling stability.

which contribute to an overall improvement in the energy storage effectiveness. (iii) The V_2CT_x@Si has better electrical conductivity and more electroactive sites, which speeds up the kinetics of the redox reaction during charging and discharging. As a result of the intercalation process, the electroactive sites of V_2CT_x@Si may be readily accessible to electrolyte ions.

Additionally, Table S1 summarizes the electrochemical performance of V_2CT_x@Si nanocomposite compared to other nanostructured electrode materials for SCs. The comparison shows that the V_2CT_x@Si nanocomposite electrode material's electrochemical performance is superior to those of previously investigated related materials.

4. Conclusion

In summary, we have presented V_2CT_x@Si nanocomposite electrode material for SC. By intercalating into the MXene interlayers, Si nanospheres serve as spacers by enlarging the ion transport channel and decreasing ion transport resistance. The V_2CT_x@Si nanocomposite electrode demonstrated remarkable charge storage capabilities, with diffusion-controlled charge storage predominating. The V_2CT_x@Si nanocomposite electrode exhibits a maximum specific capacitance of 557.7 F/g at 1 A/g. The DFT simulations demonstrated that the V_2CT_x@Si electrode material had good electronic characteristics, which led to the material's remarkable performance. These findings demonstrate that the V_2CT_x@Si possesses enhanced conductivities than the pristine V_2CT_x, which are beneficial for the rate performance of the V_2CT_x@Si nanocomposite. The obtained E_{ads} value of the V_2CT_x@Si is −0.845 eV, higher than the pristine material (−0.652 eV), indicating that it is more energetically favorable. The constructed V_2CT_x@Si//Zn can function at a wide potential range of 1.8 V and provide a high capacitance of 318.25 F/g at 1 A/g1 with a consistent cyclic life (96.4 %) up to 10,000 cycles. Furthermore, the V_2CT_x@Si//Zn has the highest energy density of 143.33 Wh/kg at a power density of 900.72 W/kg, outperforming previously reported similar work. The synergistic benefit of Si and V_2CT_x enables the V_2CT_x@Si nanocomposite to provide exceptional electrochemical performance for ZISCs.

CRediT authorship contribution statement

Abdul Mateen, **Zubair Ahmad** and **Salamat Ali**: Conceptualization, Methodology, Software, **Najam Ul Hassan**, **Fahim Ahmed**, **Razan A. Alshgari** and **Mohammed Mushab**: Data curation, Writing - Original draft preparation. **Sayed M. Eldin** and **Mohd Zahid Ansari**: Visualization, Investigation. **Mohd Zahid Ansari**, **Muhammad Sufyan Javed** and **Kui-Qing Peng**: Supervision. **Salamat Ali**, **Najam Ul Hassan**, **Fahim Ahmed**, **Razan A. Alshgari** and **Mohammed Mushab**:

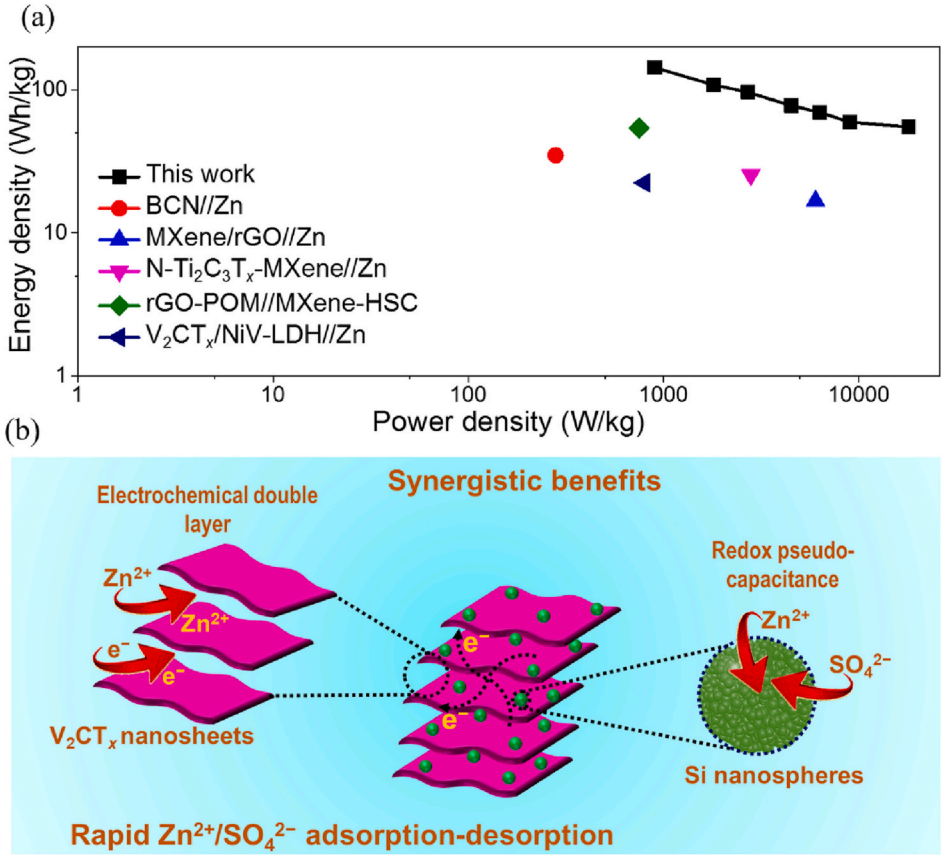

Fig. 8. (a) Ragone plot; (b) Schematic depiction of the V_2CT_x@Si electrode's charge-storage mechanism.

Software, Validation.: **Sayed M. Eldi**, **Mohd Zahid Ansari**, **Muhammad Sufyan Javed** and **Kui-Qing Peng**: Writing - Reviewing and Editing.

Declaration of competing interest

The authors declare that they have no known competing financial interests or personal relationships that could have appeared to influence the work reported in this paper.

Data availability

Data will be made available on request.

Acknowledgement

We gratefully acknowledge the financial support from the National Natural Science Foundation of China (51972031), Beijing Natural Science Foundation (2172030). This work was financially supported by the Research Fund for International Scientists (52250410342), Scientific Research start-up grant for Youth Researchers at Lanzhou University, and Supercomputing Center of Lanzhou University. This work was funded by the Researchers Supporting Project Number (RSP2023R265) King Saud University, Riyadh, Saudi Arabia. K.Q. Peng is grateful for the interdisciplinary support from Beijing Normal University.

Appendix A. Supplementary data

Supplementary data to this article can be found online at https://doi.org/10.1016/j.est.2023.108151.

References

[1] J. Yan, L. Miao, H. Duan, D. Zhu, Y. Lv, L. Li, L. Gan, M.J.C.C.L. Liu, High-energy aqueous supercapacitors enabled by N/O codoped carbon nanosheets and "water-in-salt" electrolyte, Chin. Chem. Lett. 33 (5) (2022) 2681–2686.
[2] T. Wei, J. Lu, P. Zhang, G. Yang, C. Sun, Y. Zhou, Q. Zhuang, Y.J.C.C.L. Tang, Metal–organic framework-derived Co3O4 modified nickel foam-based dendrite-free anode for robust lithium metal batteries, Chin. Chem. Lett. 34 (8) (2023), 107947.
[3] M.S. Javed, A. Mateen, S. Ali, X. Zhang, I. Hussain, M. Imran, S.S.A. Shah, W.J. S. Han, The emergence of 2D MXenes based Zn-ion batteries: recent development and prospects, Small 18 (26) (2022) 2201989.
[4] X. Li, Q. Kong, X. An, J. Zhang, Q. Wang, W. Yao, Enhanced cycling stability and storage performance of Na0.67Ni0.33Mn0.67-xTixO1.9F0.1 cathode materials by Mn-rich shells and Ti doping, J. Colloid Interface Sci. 633 (2023) 82–91.
[5] R. Ren, F. Lai, X. Lang, L. Li, C. Yao, K. Cai, Efficient sulfur host based on Sn doping to construct Fe2O3 nanospheres with high active interface structure for lithium-sulfur batteries, Appl. Surf. Sci. 613 (2023), 156003.
[6] M. Wang, C. Jiang, S. Zhang, X. Song, Y. Tang, H.-M. Cheng, Reversible calcium alloying enables a practical room-temperature rechargeable calcium-ion battery with a high discharge voltage, Nat. Chem. 10 (6) (2018) 667–672.
[7] Y. Wei, B. Tang, X. Liang, F. Zhang, Y.J.A.M. Tang, Ultrahigh mass-loading integrated free-standing functional all-carbon positive electrode prepared using architecture tailoring strategy for high-energy-density dual ion battery, Adv. Mater. (2023), 2302086.
[8] M.S. Javed, X. Zhang, S. Ali, A. Mateen, M. Idrees, M. Sajjad, S. Batool, A. Ahmad, M. Imran, T.J.N.E. Najam, Heterostructured bimetallic–sulfide@ layered Ti3C2Tx–MXene as a synergistic electrode to realize high-energy-density aqueous hybrid-supercapacitor, Nano Energy 101 (2022), 107624.
[9] X. Wang, A.Y. Mehandzhiyski, B. Arstad, K.L. Van Aken, T.S. Mathis, A. Gallegos, Z. Tian, D. Ren, E. Sheridan, B.A.J.J.o.t.A.C.S. Grimes, Selective charging behavior in an ionic mixture electrolyte-supercapacitor system for higher energy and power, J. Am. Chem. Soc. 139 (51) (2017) 18681–18687.
[10] Y. Liu, B. Fan, B. Xu, B.J.M.L. Yang, Ambient-stable polyethyleneimine functionalized Ti3C2Tx nanohybrid corrosion inhibitor for copper in alkaline electrolyte, Mater. Lett. 337 (2023), 133979.
[11] A. Mateen, M.Z. Ansari, I. Hussain, S.M. Eldin, M.D. Albaqami, A.A.A. Bahajjaj, M. S. Javed, K.-Q. Peng, Ti2CTx–MXene aerogel based ultra–stable Zn–ion supercapacitor, Composites Communications 38 (2023), 101493.

[12] J. Guo, D. Dong, J. Wang, D. Liu, X. Yu, Y. Zheng, Z. Wen, W. Lei, Y. Deng, J.J.A.F. M. Wang, Silicon-based lithium ion battery systems: state-of-the-art from half and full cell viewpoint, Adv. Funct. Mater. 31 (34) (2021) 2102546.

[13] C. Romanitan, P. Varasteanu, I. Mihalache, D. Culita, S. Somacescu, R. Pascu, E. Tanasa, S.A. Eremia, A. Boldeiu, M.J.S.R. Simion, High-performance solid state supercapacitors assembling graphene interconnected networks in porous silicon electrode by electrochemical methods using 2, 6-dihydroxynaphthalen, Sci. Rep. 8 (1) (2018) 9654.

[14] L. Zhang, W. Hao, H. Wang, L. Zhang, X. Feng, Y. Zhang, W. Chen, H. Pang, H.J.J.o. M.C.A. Zheng, Porous graphene frame supported silicon@ graphitic carbon via in situ solid-state synthesis for high-performance lithium-ion anodes, J. Mater. Chem. A 1 (26) (2013) 7601–7611.

[15] J.M. Kim, V. Guccini, D. Kim, J. Oh, S. Park, Y. Jeon, T. Hwang, G. Salazar-Alvarez, Y.J.J.o.M.C.A. Piao, A novel textile-like carbon wrapping for high-performance silicon anodes in lithium-ion batteries, J. Mater. Chem. A 6 (26) (2018) 12475–12483.

[16] S.A. Klankowski, G.P. Pandey, G.A. Malek, J. Wu, R.A. Rojeski, J.J.E.A. Li, A novel high-power battery-pseudocapacitor hybrid based on fast lithium reactions in silicon anode and titanium dioxide cathode coated on vertically aligned carbon nanofibers, Electrochim. Acta 178 (2015) 797–805.

[17] P. Lu, L. Müller, M. Hoffmann, X.J.N.E. Chen, Taper silicon nano-scaffold regulated compact integration of 1D nanocarbons for improved on-chip supercapacitor, Nano Energy 41 (2017) 618–625.

[18] R.R. Devarapalli, S. Szunerits, Y. Coffinier, M.V. Shelke, R.J.A.a.m., Boukherroub, interfaces, glucose-derived porous carbon-coated silicon nanowires as efficient electrodes for aqueous micro-supercapacitors, ACS Applied Materials Interfaces 8 (7) (2016) 4298–4302.

[19] K. Grigoras, J. Keskinen, L. Grönberg, J. Ahopelto, M. Prunnila, Coated porous Si for high performance on-chip supercapacitors, in: Journal of Physics: Conference Series, IOP Publishing, 2014, p. 012058.

[20] Y. Gogotsi, B. Anasori, The rise of MXenes, ACS Nano 13 (8) (2019) 8491–8494.

[21] B. Anasori, M.R. Lukatskaya, Y.J.N.R.M. Gogotsi, 2D metal carbides and nitrides (MXenes) for energy storage, Nature Reviews Materials 2 (2) (2017) 1–17.

[22] R. Li, L. Zhang, L. Shi, P.J.A.n. Wang, MXene Ti3C2: an effective 2D light-to-heat conversion material, ACS Nano 11 (4) (2017) 3752–3759.

[23] Z. Wang, Z. Xu, H. Huang, X. Chu, Y. Xie, D. Xiong, C. Yan, H. Zhao, H. Zhang, W.J. A.n. Yang, Unraveling and regulating self-discharge behavior of Ti3C2T x MXene-based supercapacitors, ACS Nano 14 (4) (2020) 4916–4924.

[24] A. Levitt, J. Zhang, G. Dion, Y. Gogotsi, J.M.J.A.F.M. Razal, MXene-based fibers, yarns, and fabrics for wearable energy storage devices, Adv. Funct. Mater. 30 (47) (2020) 2000739.

[25] Y. Yue, N. Liu, Y. Ma, S. Wang, W. Liu, C. Luo, H. Zhang, F. Cheng, J. Rao, X.J.A. N. Hu, Highly self-healable 3D microsupercapacitor with MXene–graphene composite aerogel, ACS Nano 12 (5) (2018) 4224–4232.

[26] M.S. Javed, A. Mateen, I. Hussain, A. Ahmad, M. Mubashir, S. Khan, M.A. Assiri, S. M. Eldin, S.S.A. Shah, W.J.E.S.M. Han, Recent progress in the design of advanced MXene/metal oxides-hybrid materials for energy storage devices, Energy Storage Materials 53 (2022) 827–872.

[27] M. Shi, R. Wang, L. Li, N. Chen, P. Xiao, C. Yan, X.J.A.F.M. Yan, Redox-active polymer integrated with MXene for ultra-stable and fast aqueous proton storage, Adv. Funct. Mater. 33 (1) (2023) 2209777.

[28] Y. Liu, J. Yu, D. Guo, Z. Li, Y.J.J.o.A. Su, Compounds, Ti3C2Tx MXene/graphene nanocomposites: synthesis and application in electrochemical energy storage, Journal of Alloys Compounds 815 (2020), 152403.

[29] J. Li, X. Yuan, C. Lin, Y. Yang, L. Xu, X. Du, J. Xie, J. Lin, J.J.A.E.M. Sun, Achieving high pseudocapacitance of 2D titanium carbide (MXene) by cation intercalation and surface modification, Adv. Energy Mater. 7 (15) (2017) 1602725.

[30] Y.T. Liu, X.D. Zhu, L.J.S. Pan, Hybrid architectures based on 2D MXenes and low-dimensional inorganic nanostructures: methods, synergies, and energy-related applications, Small 14 (51) (2018) 1803632.

[31] Q. Fan, R. Zhao, M. Yi, P. Qi, C. Chai, H. Ying, J.J.C.E.J. Hao, Ti3C2-MXene composite films functionalized with polypyrrole and ionic liquid-based microemulsion particles for supercapacitor applications, Chem. Eng. J. 428 (2022), 131107.

[32] X. Gao, X. Du, T.S. Mathis, M. Zhang, X. Wang, J. Shui, Y. Gogotsi, M.J.N.c. Xu, Maximizing ion accessibility in MXene-knotted carbon nanotube composite electrodes for high-rate electrochemical energy storage, Nat. Commun. 11 (1) (2020) 6160.

[33] X.T. Gao, Y. Xie, X.D. Zhu, K.N. Sun, X.M. Xie, Y.T. Liu, J.Y. Yu, B.J.S. Ding, Ultrathin MXene nanosheets decorated with TiO2 quantum dots as an efficient sulfur host toward fast and stable Li–S batteries, Small 14 (41) (2018) 1802443.

[34] Y.T. Liu, P. Zhang, N. Sun, B. Anasori, Q.Z. Zhu, H. Liu, Y. Gogotsi, B.J.A.M. Xu, Self-assembly of transition metal oxide nanostructures on MXene nanosheets for fast and stable lithium storage, Adv. Mater. 30 (23) (2018) 1707334.

[35] J. Wan, L. Huang, J. Wu, L. Xiong, Z. Hu, H. Yu, T. Li, J.J.A.F.M. Zhou, Microwave combustion for rapidly synthesizing pore-size-controllable porous graphene, Adv. Funct. Mater. 28 (22) (2018) 1800382.

[36] P. Hohenberg, W. Kohn, Inhomogeneous electron gas, Phys. Rev. 136 (3B) (1964) B864–B871.

[37] G. Kresse, J.J.P.r.B. Hafner, Ab initio molecular dynamics for liquid metals, Phys. Rev. B 47 (1) (1993) 558.

[38] G. Kresse, J.J.P.r.B. Furthmüller, Efficient iterative schemes for ab initio total-energy calculations using a plane-wave basis set, Phys. Rev. B 54 (16) (1996) 11169.

[39] J.P. Perdew, K. Burke, M.J.P.r.l. Ernzerhof, Generalized gradient approximation made simple, Phys. Rev. Lett. 77 (18) (1996) 3865.

[40] S. Grimme, J. Antony, S. Ehrlich, H.J.T.J.o.c.p. Krieg, A consistent and accurate ab initio parametrization of density functional dispersion correction (DFT-D) for the 94 elements H-Pu, J. Chem. Phys. 132 (15) (2010), 154104.

[41] G. Henkelman, H.J.T.J.o.c.p. Jónsson, Improved tangent estimate in the nudged elastic band method for finding minimum energy paths and saddle points, J. Chem. Phys. 113 (22) (2000) 9978–9985.

[42] M. Xia, B. Chen, F. Gu, L. Zu, M. Xu, Y. Feng, Z. Wang, H. Zhang, C. Zhang, J.J.A. n. Yang, Ti3C2T x MXene nanosheets as a robust and conductive tight on Si anodes significantly enhance electrochemical lithium storage performance, ACS Nano 14 (4) (2020) 5111–5120.

[43] H. He, Q. Xia, B. Wang, L. Wang, Q. Hu, A.J.C.C.L. Zhou, Two-dimensional vanadium carbide (V2CTx) MXene as supercapacitor electrode in seawater electrolyte, Chin. Chem. Lett. 31 (4) (2020) 984–987.

[44] Š. Masys, S. Mickevičius, S. Grebinskij, V. Jonauskas, Electronic structure of $LaNiO_{3-x}$ thin films studied by x-ray photoelectron spectroscopy and density functional theory, Phys. Rev. B 82 (16) (2010), 165120.

[45] X. Hui, R. Zhao, P. Zhang, C. Li, C. Wang, L.J.A.E.M. Yin, Low-temperature reduction strategy synthesized Si/Ti3C2 MXene composite anodes for high-performance Li-ion batteries, Adv. Energy Mater. 9 (33) (2019) 1901065.

[46] A. Gopalakrishnan, A. Yu, S.J.E. Badhulika, Fuels, facile synthesis of highly porous N-doped carbon nanosheets with silica nanoparticles for ultrahigh capacitance supercapacitors, Energy Fuel 34 (9) (2020) 11508–11518.

[47] L. Gou, W. Jing, Y. Li, M. Wang, S. Hu, H. Wang, Y.-B.J.A.A.E.M. He, Lattice-coupled Si/MXene confined by hard carbon for fast sodium-ion conduction, ACS Applied Energy Materials 4 (7) (2021) 7268–7277.

[48] Q. Liu, Y. Wang, L. Dai, J.J.A.M. Yao, Scalable fabrication of nanoporous carbon fiber films as bifunctional catalytic electrodes for flexible Zn-air batteries, Adv. Mater. 28 (15) (2016) 3000–3006.

[49] Z. Lin, D. Barbara, P.-L. Taberna, K.L. Van Aken, B. Anasori, Y. Gogotsi, P.J.J.o.P.S. Simon, Capacitance of Ti3C2Tx MXene in ionic liquid electrolyte, J. Power Sources 326 (2016) 575–579.

[50] A.S. Westover, D. Freudiger, Z.S. Gani, K. Share, L. Oakes, R.E. Carter, C.L.J. N. Pint, On-chip high power porous silicon lithium ion batteries with stable capacity over 10000 cycles, Nanoscale 7 (1) (2015) 98–103.

[51] M. Fu, Q. Zhuang, H. Yu, W.J.E.A. Chen, MnCo2S4 nanosheet arrays modified with vermicular polypyrrole for advanced free-standing flexible electrodes, Electrochim. Acta 447 (2023), 142167.

[52] A. Mateen, M.S. Javed, S. Khan, A. Saleem, M.K. Majeed, A.J. Khan, M.F. Tahir, M. A. Ahmad, M.A. Assiri, K.-Q. Peng, Metal-organic framework-derived walnut-like hierarchical Co-O-nanosheets as an advanced binder-free electrode material for flexible supercapacitor, Journal of Energy Storage 49 (2022), 104150.

[53] M.A.A. Mohd Abdah, N.H.N. Azman, S. Kulandaivalu, Y.J.S.r. Sulaiman, Asymmetric supercapacitor of functionalised electrospun carbon fibers/poly (3, 4-ethylenedioxythiophene)/manganese oxide//activated carbon with superior electrochemical performance, Sci. Rep. 9 (1) (2019) 16782.

[54] H.B. Wu, H. Pang, X.W.D.J.E. Lou, E. Science, Facile synthesis of mesoporous Ni 0.3 Co 2.7 O 4 hierarchical structures for high-performance supercapacitors, Energy Environmental Science 6 (12) (2013) 3619–3626.

[55] J. Zhang, X. Lu, J. Zhang, H. Li, B. Huang, B. Chen, J. Zhou, S.J.F.i.C. Jing, Metal-ions intercalation mechanism in layered anode from first-principles calculation, Frontiers in Chemistry 9 (2021), 677620.

[56] Y. Sun, N. Huang, D. Zhao, X. Wang, J. Zhang, S. Liu, L. Guo, X.J.C.E.J. Sun, Microwave-assisted in-situ isomorphism via introduction of Mn into CoCo2O4 for battery-supercapacitor hybrid electrode material, Chem. Eng. J. 430 (2022), 132729.

[57] C. Shi, Q. Yang, S. Chen, Y. Xue, Y. Hao, Y.J.A.A.E.M. Yan, Granular nanosheets made of interconnected NiTe2-CoTe2 nanoparticles on carbon fibers for high-performance hybrid supercapacitors, ACS Applied Energy Materials 5 (3) (2022) 2817–2825.

[58] H. Fan, X. Hu, S. Zhang, Z. Xu, G. Gao, Y. Zheng, G. Hu, Q. Chen, T.S. AlGarni, R.J. C. Luque, Flower-like carbon cathode prepared via in situ assembly for Zn-ion hybrid supercapacitors, Carbon 180 (2021) 254–264.

[59] Q. Wang, S. Wang, X. Guo, L. Ruan, N. Wei, Y. Ma, J. Li, M. Wang, W. Li, W. Zeng, MXene-reduced graphene oxide aerogel for aqueous zinc-ion hybrid supercapacitor with ultralong cycle life, Advanced Electronic Materials 5 (12) (2019) 1900537.

[60] A. Mateen, M.Z. Ansari, Q. Abbas, A. Muneeb, A. Hussain, E.T. Eldin, F. M. Alzahrani, N.S. Alsaiari, S. Ali, M.S. Javed, In situ nitrogen functionalization of 2D-Ti3C2T x-MXenes for high-performance Zn-ion supercapacitor, Molecules 27 (21) (2022) 7446.

[61] S.-K. Hwang, S.J. Patil, N.R. Chodankar, Y.S. Huh, Y.-K. Han, An aqueous high-performance hybrid supercapacitor with MXene and polyoxometalates electrodes, Chem. Eng. J. 427 (2022), 131854.

[62] J. Pan, S. Li, L. Zhang, F. Li, Z. Zhang, T. Yu, D.J.J.o.E.S. Zhang, Designed formation of 2D/2D hierarchical V2CTx MXene/NiV layered double hydroxide heterostructure with boosted electrochemical performance for asymmetric supercapacitors, Journal of Energy Storage 55 (2022), 105415.